8-1-2009

Impact of Hillslope-Scale Organization of Topography, Soil Moisture, Soil Temperature, and Vegetation on Modeling Surface Microwave Radiation Emission

Alejandro N. Flores
Boise State University

Valeriy Y. Ivanov
University of Michigan

Dara Entekhabi
Massachusetts Institute of Technology

Rafael L. Bras
University of California, Irvine

Impact of Hillslope-Scale Organization of Topography, Soil Moisture, Soil Temperature, and Vegetation on Modeling Surface Microwave Radiation Emission

Alejandro N. Flores, *Member, IEEE*, Valeriy Y. Ivanov, Dara Entekhabi, *Senior Member, IEEE*, and Rafael L. Bras

***Abstract*—Microwave radiometry will emerge as an important tool for global remote sensing of near-surface soil moisture in the coming decade. In this modeling study, we find that hillslope-scale topography (tens of meters) influences microwave brightness temperatures in a way that produces bias at coarser scales (kilometers). The physics underlying soil moisture remote sensing suggests that the effects of topography on brightness temperature observations are twofold: 1) the spatial distribution of vegetation, moisture, and surface and canopy temperature depends on topography and 2) topography determines the incidence angle and polarization rotation that the observing sensor makes with the local land surface. Here, we incorporate the important correlations between factors that affect emission (e.g., moisture, temperature, and vegetation) and topographic slope and aspect. Inputs to the radiative transfer model are obtained at hillslope scales from a mass-, energy-, and carbon-balance-resolving ecohydrology model. Local incidence and polarization rotation angles are explicitly computed, with knowledge of the local terrain slope and aspect as well as the sky position of the sensor. We investigate both the spatial organization of hillslope-scale brightness temperatures and the sensitivity of spatially aggregated brightness temperatures to satellite sky position. For one computational domain considered, hillslope-scale brightness temperatures vary from approximately 121 to 317 K in the horizontal polarization and from approximately 117 to 320 K in the vertical polarization. Including hillslope-scale heterogeneity in factors effecting emission can change watershed-aggregated brightness temperature by more than 2 K, depending on topographic ruggedness. These findings have implications for soil moisture data assimilation and disaggregation of brightness temperature observations to hillslope scales.**

***Index Terms*—Ecohydrology, microwave radiometer, observation bias, radiative transfer, remote sensing, soil moisture, soil temperature, topography, vegetation.**

Manuscript received March 17, 2008; revised June 27, 2008, August 17, 2008, and December 11, 2008. First published April 10, 2009; current version published July 23, 2009. This work was supported in part by Army Research Office under Grant W911NF-04-1-0119 and in part by the National Aeronautics and Space Administration under Grant NNG05GA17G.

A. N. Flores is with the Geosciences Department, Boise State University, Boise, ID 83725 USA (e-mail: lejoflores@boisestate.edu).

V. Y. Ivanov is with the Department of Civil and Environmental Engineering, University of Michigan, Ann Arbor, MI 48109 USA.

D. Entekhabi is with the Department of Civil and Environmental Engineering and the Department of Earth, Atmospheric, and Planetary Sciences, Massachusetts Institute of Technology, Cambridge, MA 02139-4307 USA.

R. L. Bras is with the Henry Samueli School of Engineering, University of California, Irvine, CA 92697 USA.

Digital Object Identifier 10.1109/TGRS.2009.2014743

I. Introduction

SPACEBORNE and airborne radiometric sensing is emerging as the primary tool for observing the hydrologic state of the Earth's system. Microwave radiometry is particularly useful for near-surface soil moisture estimation because the dielectric constant, and therefore emissivity, of soils varies significantly with moisture content in the lower microwave region of the electromagnetic spectrum (i.e., 1–6 GHz) [1]–[5]. L-band microwave radiometry technology is vital to both the European Space Agency's Soil Moisture and Ocean Salinity (SMOS) mission, which is scheduled to launch in 2008 [6], [7], and the National Aeronautics and Space Administration's Soil Moisture Active–Passive (SMAP) mission, which is scheduled to launch between 2010 and 2013 (http://smap.jpl.nasa.gov/). For a loamy soil with sparse natural grass cover, a change in brightness temperature of 10 K in both horizontal and vertical polarizations is associated approximately with an 8% and change in volumetric water content at incidence angles θ ranging from 40° to 60° [1], [8], [9]. This range of incidence angles coincides with off-nadir look angles of existing and planned radiometers [2], [4], [6], [7]. Estimates of near-surface soil moisture are typically retrieved from observations (in the form of brightness temperature images) through numerical inversion of a radiative transfer model (RTM) [6], [7], [10]. Formulation of soil moisture retrieval algorithms requires approximate inversion of a nonlinear RTM that simulates synthetic brightness temperature observations at the satellite from known inputs. Inputs to the RTM are typically spatial maps of near-surface moisture and temperature, along with ancillary data related to surface vegetation conditions and soil roughness. The moisture and temperature states input to the RTM are often derived from physically based land surface models. Microwave radiometry is also a component critical to the related area of land surface data assimilation, which employs algorithms to constrain observations of brightness temperatures to physically based land surface models. In soil moisture data assimilation, the RTM serves as the observing system that projects the modeled states from state to observation space [11], [12].

Previous studies requiring extensive RTM use typically resolve the land surface at resolutions coarser than 1 km [2], [5], [10], [13], [14]. However, it has been well established that the spatial distribution of inputs to existing RTMs, specifically soil

moisture, vary significantly over a range of spatial scales [15]–[17]. Variation at the hillslope scale (tens of meters) is associated with spatial variability of topography, soil, and vegetation [18]. In these studies, spatial variation in soil moisture and vegetation states at hillslope scales has largely been ignored. This is primarily because models that are capable of resolving moisture and vegetation states at these scales (referred to hereafter as watershed-scale models) are of intractably high dimension when considering a spatial domain of sufficient size to develop soil moisture retrieval algorithms. In addition to influencing hydrology and vegetation, local topography dictates the local incidence and polarization rotation angles, to which observed brightness temperatures are sensitive [1], [8], [9], [19]. The impact of topography on viewing geometry is increasingly gaining attention in the remote sensing literature [19]–[23]. In a modeling study using digital elevation models (DEMs), Kerr *et al.* [20] find that modeled brightness temperatures in areas of variable topography can be several kelvins different than a corresponding flat surface. Talone *et al.* [21] used a 30-m DEM and a 100-m land cover map to derive inputs to the SMOS RTM, in which the DEM is used to incorporate topographic effects on shadowing and local incidence angles. Further, Mialon *et al.* [22] recently discussed these effects in the context of the SMOS mission and developed a criterion to identify SMOS brightness temperature pixels in which topographic effects on incidence angle are likely to result in observation errors greater than the required 4-K accuracy [3]. The works of Sandells *et al.* [23] and Mätzler and Standley [19] are notable because they include the effects of topographic slope on the geometry of observation; they did not consider the covariation between topography and the land surface factors affecting emission of microwave energy.

This paper aims at demonstrating the effect of topographic variability, vis-á-vis its relationship to observation geometry and surface states, in modeling microwave radiation emission from soils. A topography-dependent spatially distributed mass-, energy-, and carbon-balance-resolving watershed model [24]–[28] is used to generate the soil and vegetation states required as input to an RTM for two semiarid watersheds. The model includes a dynamic ecology component as well as full water and energy balance (with radiative exchanges). The model can hence produce correlations between slope, aspect, and factors that affect the emission of microwave energy at the surface, such as soil moisture, soil temperature, and vegetation biomass. Incidence angle and polarization rotation are computed at every computational element in the modeling domain, with knowledge of the slope and aspect as well as the relative sky position of the synthetic sensor. By allowing the local incidence angle, polarization rotation, vegetation biomass, canopy temperature, soil moisture, and soil temperature to vary spatially at hillslope scales, we demonstrate that topography significantly affects the spatial distribution of modeled brightness temperature. In a manner similar to the works of Mätzler and Standley [19] and Sandells *et al.* [23], and because there are currently no spaceborne L-band microwave measurements, this work focuses on quantifying the sensitivity of modeled microwave brightness temperatures to topographic variation in a set of synthetic landscapes.

A description of the physical theory underlying modeling microwave radiation emission from soils follows in Section II. Section III demonstrates that hillslope-scale heterogeneity significantly influences the spatial distribution of predicted brightness temperatures. When aggregated to a spatial scale of 2 km, the predicted brightness temperature observations exhibit significant sensitivity to the relative sky position of the observing platform. To infer potential effects of topography at the scale of satellite observation, we compare empirical frequency distributions of incidence angles derived from 10-m-resolution DEMs at scales of 10, 25, and 40 km. Implications of this work for applications involving surface microwave emission modeling, including brightness temperature disaggregation and data assimilation, are discussed in Section IV.

II. Modeling Microwave Radiation Emission

A. RTM

Emission of microwave radiation from the Earth's surface is modeled through a layered single-scattering RTM [29]. The predicted observation of brightness temperature (T_{bp}) observed by the sensor at polarization p is comprised of a component from a vegetated fractional area (f_c) and a component from the bare soil ($1 - f_c$), as presented by Crow *et al.* [10] as follows:

$$T_{bp} = f_c \left\{ T_S e_p \exp\left(-\frac{\tau_p}{\cos\theta}\right) + T_C(1-\omega_p)\left(1-\exp\left(-\frac{\tau_p}{\cos\theta}\right)\right) \cdot \left(1 + r_p \exp\left(-\frac{\tau_p}{\cos\theta}\right)\right)\right\} + (1-f_c) T_S e_p \quad (1)$$

where e_p is the emissivity of the soil (dimensionless), τ_p is the nadir vegetation opacity (in nepers) at polarization p, θ is the local incidence angle (in radians), T_C and T_S are the canopy and soil temperatures (in kelvins), ω_p is the single-scattering albedo (dimensionless) at polarization p, and r_p is the local reflectivity of the soil ($r_p = 1 - e_p$) (dimensionless). The $-\tau_p/\cos\theta$ term in (1) is a theoretical representation for the vegetation opacity, taking into account the slant path through the vegetation layer [1] originally formulated by Kirdiashev *et al.* [30] and later derived using effective medium theory [31].

Vegetation opacity τ_p varies by plant type and is often modeled as a linear function of vegetation water content V_{wc} (in kilograms per square meter) in which the constant of proportionality b_p is a vegetation type-dependent opacity coefficient [32], [33] that depends on polarization, i.e.,

$$\tau_p = b_p V_{wc}. \quad (2)$$

Because this paper focuses on semiarid landscapes with natural grasses, vegetation water content is estimated through an empirical linear relationship between V_{wc} and leaf area index (LAI) based on field data suggested by de Rosnay *et al.* [34] for semiarid grasses. We have

$$V_{wc} = 0.37\,\mathrm{LAI} + 0.123. \quad (3)$$

In the semiarid grassland considered, simulated fractional vegetation cover is approximately 34%, maximum LAI is approximately 0.94, and maximum vegetation height is approximately 0.24 m. Undisturbed natural grasses are primarily oriented vertically, which could lead to significant polarization effects. However, several studies have found that these polarization effects are small in grasslands similar to the ones considered here [10], [35], [36], and we neglect the polarization effects on τ_p, b_p, and ω_p. However, it should be noted that Schwank *et al.* [37] conclude that anisotropic vegetation models are most appropriate in soil moisture retrieval algorithms because of the anisotropic nature of real canopies. Importantly, in a series of field experiments in forested areas Guglielmetti *et al.* [38] concluded that significant canopy cover can significantly attenuate the moisture signal from the ground surface.

The inputs to the RTM, namely, T_S, T_C, ω, V_{wc}(LAI), b, h, and m_v, characterize the state of land surface soil and vegetation. These states can be evolved by a spatially distributed physically based watershed model that takes hydrometeorological forcings as input. The nature of the watershed model used in this study are described in more detail later in this paper.

B. Dependence of Observation Geometry on Topography

Both scattering geometry and polarization are affected by topography [19]. Particularly, previous experimental studies have found that T_{bp} is particularly sensitive to θ [1], [8], [9]. At a location R at which the emission of microwave radiation is modeled, the position of an observing satellite S relative to the reference location can be expressed as a function of the azimuth (ζ_S) and zenith (δ_S) angles from the reference to the satellite (Fig. 1). By convention, ζ_S is defined as the angle made between the locally horizontal line connecting R with true north and the locally horizontal line connecting R with the subsatellite point (the point on the Earth's surface directly beneath the satellite), positive clockwise. δ_S is the angle between a line originating at R in the $-g$-direction and the line connecting R and the satellite S and can be approximated as the off-nadir look angle of the sensor. For a sloping surface, the local incidence angle that the observing satellite makes with the reference location is a function of the local topographic slope (α_∇) and aspect (ζ_∇) (Fig. 1). By convention, ζ_∇ is defined as the angle in the locally horizontal plane that the local direction of steepest descent makes with true north. α_∇ is the local gradient with respect to the horizontal in the direction of steepest descent. The local incidence angle θ can be computed, with knowledge of the values of ζ_S, ζ_∇, δ_S, and α_∇, through the spherical law of cosines [19], i.e.,

$$\cos\theta = \cos\alpha_\nabla \cos\delta_S + \sin\alpha_\nabla \sin\delta_S \cos(\zeta_S - \zeta_\nabla). \quad (4)$$

Surface topography also results in a rotation of the linear polarization by an angle φ and, following the work of Mätzler and Standley [19], is calculated as

$$\sin\varphi = \sin(\zeta_S - \zeta_\nabla)\sin\alpha_\nabla / \sin\theta. \quad (5)$$

The polarization-dependent reflectivity from (1), represented by r_p, is computed as the reflectivity of an equivalent smooth surface r_{sp} extinguished exponentially as a function of the parameter h, which is linearly related to the root-mean-square surface height, i.e.,

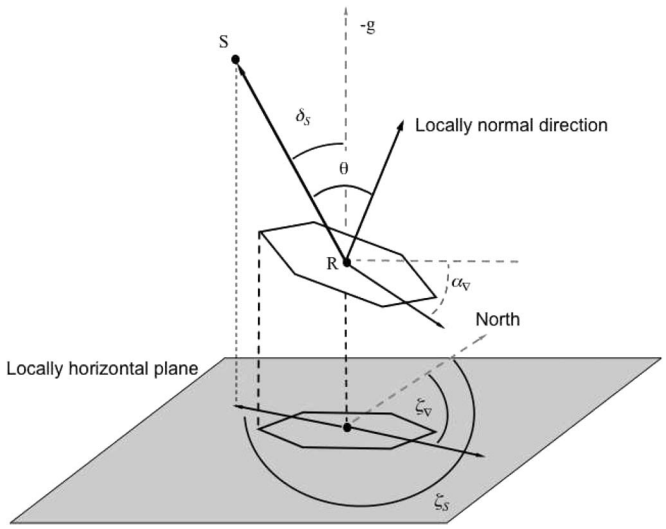

Fig. 1. Definition of topographic slope α_∇ and aspect ζ_∇ at location R and relation to satellite sky position S, as characterized by the azimuth angle to the satellite ζ_S and the zenith angle to the satellite δ_S.

$$r_p = r_{sp}\exp(-h). \quad (6)$$

The parameter h in (6) is meant to capture the effects of soil microtopographic variation on the reflectivity. The reflectivity of the smooth surface r_{sp} is a function of the dielectric constant of the soil–air–water matrix ϵ_{eff} and the local incidence angle θ. Following the formulation outlined in [19], the horizontally polarized reflectivity in the reference frame of the observing sensor r_{sh} can be determined as a function of the linear polarization rotation angle φ, i.e.,

$$r_{sh} = r_{sh,l}\cos^2\varphi + r_{sv,l}\sin^2\varphi. \quad (7)$$

Similarly, the vertically polarized reflectivity in the observing sensor reference frame r_{sv} can be determined as

$$r_{sv} = r_{sv,l}\cos^2\varphi + r_{sh,l}\sin^2\varphi. \quad (8)$$

In (7) and (8), $r_{sh,l}$ and $r_{sv,l}$ are the horizontally polarized and vertically polarized smooth surface reflectivity in the local reference frame, respectively, and are determined through the Fresnel equations [39]. For $p = h$, we have

$$r_{sh,l} = \left|\frac{\cos\theta - \sqrt{\epsilon_{\text{eff}} - \sin^2\theta}}{\cos\theta + \sqrt{\epsilon_{\text{eff}} - \sin^2\theta}}\right|^2. \quad (9)$$

For $p = v$, we have

$$r_{sv,l} = \left|\frac{\epsilon_{\text{eff}}\cos\theta - \sqrt{\epsilon_{\text{eff}} - \sin^2\theta}}{\epsilon_{\text{eff}}\cos\theta + \sqrt{\epsilon_{\text{eff}} - \sin^2\theta}}\right|^2. \quad (10)$$

In (9) and (10), ϵ_{eff} is the effective dielectric constant of the soil–water–air medium. Formulation and validation of conceptual soil models describing the dielectric behavior of

soils as a function of physical and chemical properties and degree of wetness have a long history and remain as an active area of research [40]–[44]. Such models often describe the behavior of both the real and complex parts of the dielectric constant and may include the effects of high ion concentrations at low moisture contents associated with clay-rich soils. These models are desirable insofar as the relationship between dielectric constant and soil moisture varies by soil type (i.e., clay, silt, loam), and they are more generally applicable over regions with significant heterogeneity in soil characteristics. However, they introduce additional parameters that often must be determined through detailed laboratory characterization of soils (e.g., cation exchange capacity). For the purposes of this work, we use the following simple frequently used empirical relationship that describes the effective dielectric constant as a function of volumetric soil moisture content only [45]:

$$\epsilon_{\text{eff}} = 3.03 + 9.3m_v + 146m_v^2 - 76.7m_v^3 \qquad (11)$$

where m_v is the volumetric soil moisture (in cubic meters per cubic meter). Though empirical, this equation approximates well the effective dielectric constant for mineral soils [42].

To summarize, (4) and (5) provide the mathematical framework by which the local incidence angle and polarization rotation can, with knowledge of the sky position of the observing sensor contained in δ_S and ζ_S, be computed through terrain analysis of topographic data.

C. Land Surface Ecohydrology Modeling

The hillslope-scale distributions of m_v, T_S, T_C, and LAI required as input to the RTM are obtained using the coupled Triangulated Irregular Network (TIN)-based Realtime Integrated Basin Simulator (tRIBS) [24], [25], and [46] coupled to the VEGetation Integrated Evolution (VEGGIE) model [26]–[28], hereafter referred to as tRIBS–VEGGIE. tRIBS–VEGGIE is a spatially distributed model that resolves mass, energy, and carbon balance over a watershed at the hillslope scale by representation of coupled 1) biophysical energy processes (e.g., partitioning of input solar radiation in the canopy and soils), 2) biophysical hydrologic processes (partitioning of rainfall into interception, throughfall, plant water uptake, etc.), and 3) biochemical processes and vegetation phenology. A full treatment of the tRIBS–VEGGIE model is beyond the scope of this paper, and the reader is directed to previous studies describing the development, parameterization, and confirmation of the tRIBS–VEGGIE framework [24]–[28], [46]. What follows in this section is a brief description of the soil moisture modeling component, the vegetation dynamics embodied by the model, and an overview of the static data required to simulate the near-surface moisture, temperature, and vegetation variable used as input to the RTM.

Infiltration of water into the soil is modeled using a 1-D Richards equation for a sloped surface that allows for lateral gravitational drainage. The lower boundary condition of the model is a flux boundary condition, consistent with the assumption of significant depth to the saturated subsurface in the semiarid environment for which the model is currently parameterized. The Brooks–Corey model [47] is used to characterize the relationship between soil moisture and hydraulic conductivity and between soil moisture and matric potential. Slope-parallel hydraulic conductivity is proportional to the slope-normal hydraulic conductivity by a factor termed the anisotropy ratio.

TABLE I
RANGE OF LAND SURFACE STATE INPUTS TO AN RTM FOR DIFFUSIVE AND FLUVIAL EROSION DOMAINS

	Diffusive erosion landscape		Fluvial erosion landscape	
Variable	Mean	Range	Mean	Range
T_S [K]	324.68	318.82-327.22	321.66	310.13-327.29
T_C [K]	314.77	311.48-316.32	313.01	306.67-316.43
f_c [m^2/m^2]	0.342	0.311-0.378	0.337	0.265-0.390
m_v [m^3/m^3]	0.0291	0.0287-0.0297	0.0291	0.0286-0.0299
LAI [m^2/m^2]	0.799	0.711-0.904	0.783	0.586-0.940
h [-]	0.10			
b [-]	0.10			
ω [-]	0.05			

The dynamic vegetation component of tRIBS–VEGGIE operates on specified plant functional types (PFTs) [48]. For each PFT, tRIBS–VEGGIE simulates carbon fluxes by representing the processes of photosynthesis, autotrophic respiration, stress induced foliage loss, and tissue turnover. The fluxes that determine the exchange of CO_2 between the atmosphere and the land surface contribute to the dynamics in the following three carbon pools modeled within tRIBS–VEGGIE: 1) foliage; 2) sapwood; and 3) fine roots. Assimilation of CO_2 through photosynthesis is coupled to surface energy and water balance through the stomatal resistance model, which depends on the budget of long-wave and solar radiation and site soil moisture throughout the rooting profile of the PFT. The amount of incoming solar radiation being received at any time during the day at the land surface depends on site slope and aspect, as well as on the solar azimuth angle. In this manner, tRIBS–VEGGIE simulates the spatial covariation between incident solar radiation and surface moisture, energy, and plant vigor processes, which leads to north- and south-facing contrasts in variables such as surface temperature, canopy temperature, and available energy. As part of model calibration and confirmation, Ivanov *et al.* [27] demonstrate that tRIBS–VEGGIE is capable of reproducing point-scale observations of vegetation biomass obtained at several irregularly spaced times over several growing seasons at the Sevilleta National Wildlife Refuge.

Hydrologic and vegetation states input to the RTM are obtained from the spatially distributed simulations thoroughly presented in [27]. The following variables from [26] were used as input to the RTM: 1) soil moisture in the top 25 mm of the soil column (m_v); 2) soil temperature (T_S); 3) canopy temperature (T_C); and 4) LAI. Vegetation water content (V_{wc}) was computed from (3) with the simulated LAI, and the effective dielectric constant (ϵ_{eff}) was computed from (11) with the simulated volumetric soil moisture (m_v). Values of the parameters ω, h, and b are taken from [10] for the short grass landuse cover type. Values of the inputs to the RTM are summarized in Table I for the two watersheds considered in this paper.

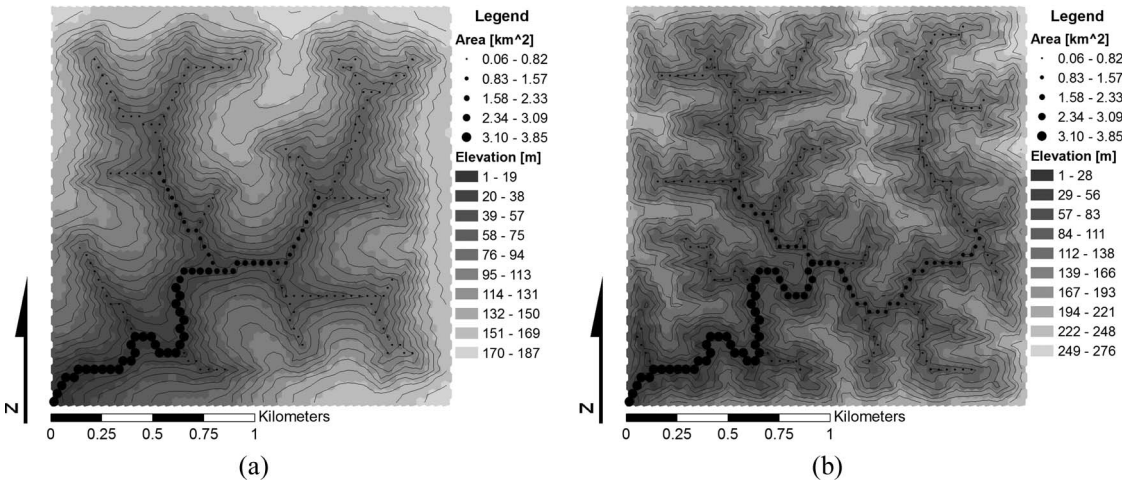

Fig. 2. Two catchments used as computational domains for tRIBS–VEGGIE and generated by a physically based landscape evolution model with (a) slope-dependent diffusive erosion resulting in landscape less dissected by channels with longer hillslopes and shallower slopes (average and standard deviation in slope is 0.231 and 0.103 m/m, respectively) and (b) overland flow-dependent fluvial erosion resulting in more channel dissection of the landscape, shorter hillslopes, and higher slopes (average and standard deviation in slope is 0.500 and 0.192 m/m, respectively). Black circles represent the channel network and are proportional in size to upstream contributing area (in square kilometers). Black lines are elevation contours and are drawn at 10-m intervals in the diffusion domain and 20-m intervals in the fluvial domain.

Inputs to the tRIBS–VEGGIE model correspond to the following four categories of data: 1) hourly hydrometeorological forcings; 2) soil hydraulic and thermal properties; 3) vegetation parameters; and 4) a static elevation field representing watershed topography. Hydrometeorological forcings for tRIBS–VEGGIE include hourly 1) precipitation; 2) sky fractional cover or incoming solar radiation; 3) air temperature; 4) dew temperature; and 5) wind speed. In this study, hydrometeorological forcings under which the moisture and vegetation state are evolved by tRIBS–VEGGIE were generated by a stochastic weather generator [28]. Soil hydraulic and thermal parameters are consistent with those common to many land surface models (e.g., [49]–[53]) and available in published soil databases such as the STATSGO or SSURGO products. Soil parameters required for water- and energy-balance solution include the following: 1) saturated hydraulic conductivity; 2) saturation moisture content; 3) residual moisture content; 4) Brooks–Corey parameters; 5) specific volumetric heat capacity; and 6) thermal conductivity. Here, we assume a loamy soil that is spatially homogeneous throughout the watersheds considered. Parameters required by the vegetation development model coincide with the C4 grass PFT parameterized in other biophysical–biochemical models (e.g., see [54]–[58]). Watershed topography is represented as a network of Voronoi polygons derived from a TIN representation of input static DEMs such as those from the Shuttle Radar Topography Mission [59]. The elevation TIN representations of the two watersheds considered in this paper were constructed using a process-based landscape development model and are described in the following section.

D. Topographic Boundary Conditions

Two contrasting elevation fields are used as static topographic boundary conditions for tRIBS–VEGGIE in this study. The distinct elevation fields vary in degree of slope variability, which is important for the study tests, and were generated by a physically based landscape evolution model that evolves local elevation as a function of sediment influx and outflux [60]–[62]. The landscape evolution model has previously been shown to reproduce equilibrium slope-contributing area scaling relationships observed in real landscapes [61]. Each domain is 2×2 km and contains 2401 equally spaced computational facets. The two simulated domains correspond to two different dominating erosional mechanisms. A diffusive erosion terrain assumes that slope-dependent processes (e.g., soil creep) are the primary mechanism of erosion locally, resulting in shallower slopes, longer hillslopes, and lower topographic relief (range in watershed elevation) [Fig. 2(a)]. The fluvial erosion terrain assumes that the primary mechanism of local erosion is shear stress above some threshold imparted by surface runoff, resulting in higher slopes, shorter hillslopes, and greater topographic relief [Fig. 2(b)]. Ivanov *et al.* [26], [27] use the diffusive erosion and fluvial erosion synthetic terrains as the geometric constructs for several multiyear simulations to develop patterns of soil moisture and vegetation biomass consistent with field-based observations. The use of these synthetic domains allows, through tRIBS–VEGGIE, the generation of RTM inputs that are known to be completely internally consistent and causally linked. By examining these ideal but realistic cases, this study seeks to illuminate the sensitivity of microwave brightness temperature observations, as predicted by a widely used RTM.

In both of these domains and at each computational cell, the local incidence angle (θ) is computed with (4), and the polarization rotation (φ) is computed with (5), given the local slope (α_∇) and aspect (ζ_∇), and assumed values for satellite azimuth (ζ_S) and satellite zenith (δ_S). In the following examples, the satellite zenith angle is assumed to be equal to 40°, which is consistent with conceived soil moisture sensing platforms (e.g., [3], [4], [6], [7], [10]). Furthermore, we assume the value of ζ_S to be 150° from the north (positive clockwise), which is close

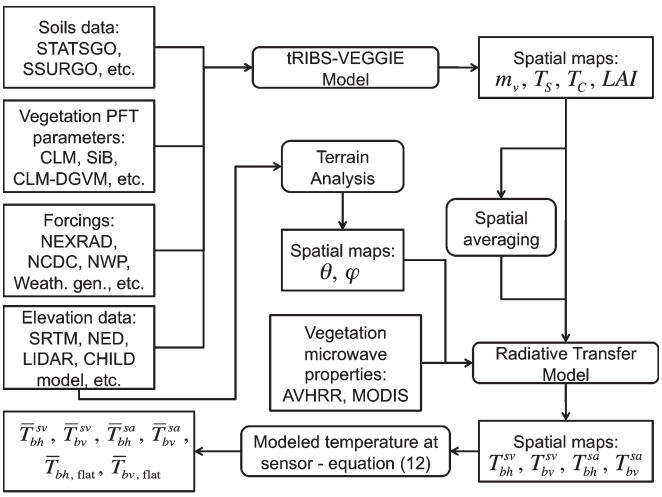

Fig. 3. Flowchart depicting the data required to model the emission of microwave radiation at hillslope scales using the tRIBS–VEGGIE model.

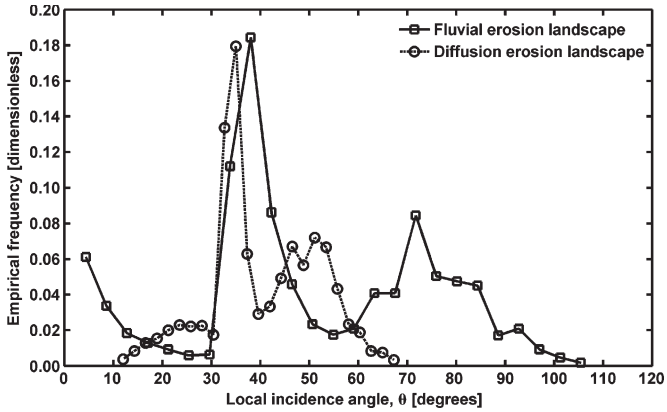

Fig. 4. Empirical frequency distributions of incidence angle (θ), assuming $\zeta_S = 150^\circ$ and $\delta_S = 40^\circ$ for fluvial (solid line marked by open squares) and diffusive (dashed line marked by open circles) erosion domains.

to the azimuth that would be encountered during the ascending limb of a soil moisture sensing satellite in a Sun-synchronous orbit in middle latitudes (e.g., [2]).

In this modeling study, we are interested in investigating both hillslope-scale characteristics affecting emission of microwave energy at the surface and in how the organization of those factors impact the aggregated brightness temperature. The spatial extent of the domains considered in this study is significantly smaller than the scale of existing and planned brightness temperature products (e.g., 2 km versus 40 km, respectively). Generating significantly larger landscapes with sufficient topographic detail (e.g., larger than 10 km $\times$ 10 km in spatial extent at spatial resolutions of 90 m or finer) is computationally difficult. Moreover, it is reasonable to assume that for the relatively dry and clear conditions considered, the ecohydrological states simulated by tRIBS–VEGGIE for the small landscape would exhibit similar spatial organization of hillslope-scale soil moisture, soil temperature, and vegetation characteristics affecting microwave energy emission as those at larger spatial scales. That is, the 2 km $\times$ 2 km region is assumed to be representative of a larger area of relatively homogeneous ecohydrologic and topographic variability. Therefore, our interpretations of radiative transfer modeling results with the 2 km $\times$ 2 km domains are believed qualitatively inferential for a domain up to the size of one radiometer pixel, provided that such a domain exhibits relatively consistent topographic, vegetative, and hydrologic variability. It should also be noted that we do not mask locations within each domain that may be obscured from satellite observation by surrounding terrain. Incorporating these effects on visible sky is a straightforward extension of this work: emission of microwave radiation is simply not modeled at computational elements obscured from view of the satellite by surrounding terrain (e.g., see [19] for a discussion of one parametric technique for incorporating these effects). The models and data required for the microwave emission modeling performed in this study is illustrated through a flowchart in Fig. 3.

III. Results

A. Spatial Organization of Hillslope-Scale Brightness Temperatures

The assumed values for ζ_S and δ_S are 150° and 40°, respectively. This implies that hillslopes with aspects oriented toward the observing sensor (south- to southeast-facing hillslopes in this case) possess the lowest values of θ within the domain. Conversely, hillslopes with aspects oriented away from the sensor (north- to northwest-facing hillslopes) would possess highest values of θ. Instantaneous values of the land surface state inputs to (1) are obtained from a tRIBS–VEGGIE model simulation corresponding to a hypothetical midday on August 14 with no rain or clouds. A preliminary sensitivity analysis of the dependence of brightness temperature on incidence angle (e.g., similar to that of [1], [8], and [9]) reveals that for $65^\circ \leq \theta < 90^\circ$, the brightness temperature decreases rapidly in the vertical polarization as θ approaches 90° for surface conditions corresponding to mean values in Table I. Moreover, for $65^\circ \leq \theta < 90^\circ$, increasing volumetric soil moisture is associated with increasing T_{bv}. In the diffusive erosion domain, few hillslopes exhibit $\theta \geq 65^\circ$ (Fig. 4) and T_{bv} increases monotonically with θ in this domain for given surface states. In the fluvial erosion domain, by contrast, a significant number of hillslopes exhibit $\theta \geq 65^\circ$ (Fig. 4). Hence, for the assumed satellite position, the fluvial domain contains areas with θ such that T_{bv} decreases with increasing volumetric soil moisture (i.e., $\theta \leq 65^\circ$) and areas with θ such that T_{bv} increases with increasing volumetric soil moisture (i.e., $\theta \geq 65^\circ$).

As previously stated, for the two synthetic domains, spatially varying inputs to the RTM represent instantaneous values of local T_S, T_C, V_{wc}, h, and m_v simulated by tRIBS–VEGGIE during a rain-free day in mid-August. Again, the range of variability of each state variable input to the radiative transfer scheme for both domains is given in Table I. The spatial organization of factors affecting emission impact the spatial distribution of hillslope-scale brightness temperatures in a significant and consistent manner (Fig. 5). While the organization of near-surface soil moisture, soil temperature, canopy temperature, and vegetation height and abundance (as modulated by the

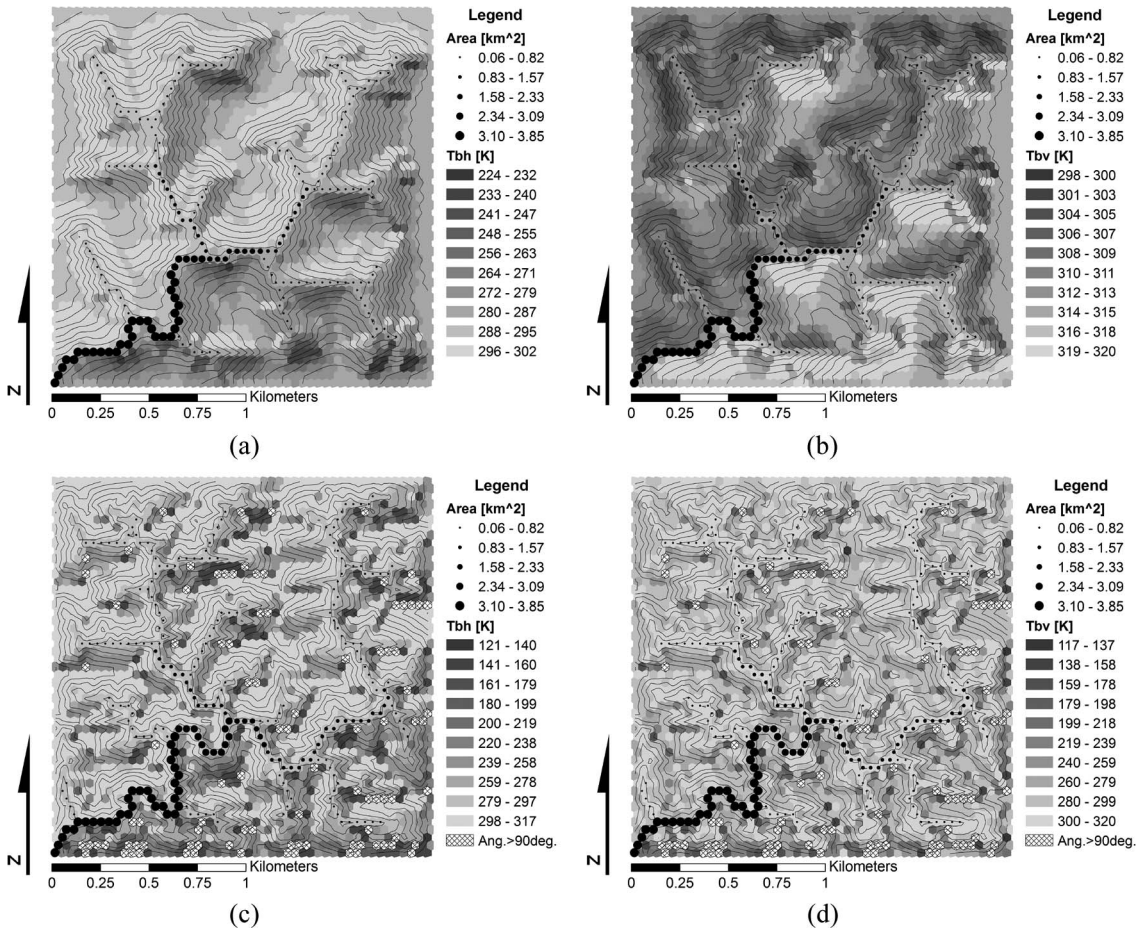

Fig. 5. Spatial distribution of brightness temperature, assuming $\zeta_S = 150^\circ$ and $\delta_S = 40^\circ$ with land surface states at each pixel evolved by the tRIBS–VEGGIE model for (a) diffusion-dominated terrain in the horizontal polarization, (b) diffusion-dominated terrain in the vertical polarization, (c) fluvial-erosion-dominated terrain in the horizontal polarization, and (d) fluvial-erosion-dominated terrain in the vertical polarization. Note that brightness temperatures in (c) and (d) are plotted in geometric intervals due to the large range of variability.

effect of LAI on vegetation optical thickness) all generically impact the hillslope-scale distribution of modeled brightness temperatures, in Fig. 5, it is the spatial variability in surface temperature and the impact of topography on observing geometry that most significantly influence the distribution of brightness temperatures. In the diffusive erosion landscape, the range of modeled brightness temperatures varies from approximately 224 to 302 K in the horizontal polarization [Fig. 5(a)] and from approximately 298 to 320 K in the vertical polarization [Fig. 5(b)]. Computational pixels with west- and north-facing aspects exhibit lower T_{bh} relative to south- and east-facing pixels. Alternatively, south- and east-facing pixels tend to exhibit lower T_{bv} than pixels facing north and west. Similar patterns to those seen in the diffusive erosion domain can be seen in the fluvial erosion domain, though the scale of spatial variation in modeled brightness temperatures is finer than in the diffusive erosion domain and the range of variability in brightness temperature higher. There exist computational elements within the fluvial erosion domain that cannot be observed because the local value of θ would be greater than 90°, given the assumed ζ_S and δ_S and local values of α_∇ and ζ_∇. In the fluvial erosion landscape, the range of modeled brightness temperatures varies from approximately 121 to 317 K in the horizontal polarization [Fig. 5(c)] and from approximately 117 to 320 K in the vertical polarization [Fig. 5(d)]. Similar to the diffusive erosion domain, north- and west-facing hillslopes in the fluvial erosion domain are associated with the lowest values of T_{bh}. Explaining the spatial distribution of T_{bv} in the fluvial erosion domain is more difficult since the distribution of θ within the domain results in areas where T_{bv} increases with m_v, T_S, and T_C and areas where T_{bv} decreases with increasing m_v, T_S, and T_C. Spatial patterns of hillslope-scale T_{bh} and T_{bv} in both domains are associated with both topography-controlled variation on incidence angles and surface states.

Topographic controls on the distribution of incoming solar radiation lead to tendencies of south- and southeast-facing hillslopes to exhibit higher soil temperatures, lower moisture, and lower vegetation biomass (in the Northern Hemisphere). The tendency for lower moisture and higher soil temperatures in these areas would lead to higher values of T_{bh} for given θ. On the other hand, north- and northwest-facing hillslopes are exposed to less incident solar radiation and therefore tend to exhibit lower daytime soil and canopy temperatures, higher soil moisture, and greater vegetation biomass than south-facing hillslopes. Therefore, topographic gradients in surface states act to enhance north–south contrasts in hillslope-scale T_{bh} compared with topographic effects on incidence angle alone for the assumed ζ_S and δ_S.

Given the simulated dry and sparsely vegetated conditions in this study, the range in modeled brightness temperatures in both computational domains and polarizations is primarily attributable to both spatial variability in emissivity and soil surface temperature. Because the range of variation in T_{bp} is substantially greater than the range of variation in T_S, we conclude that significant spatial variation in emissivity exists within the simulated domains. Despite an almost spatially uniform dielectric constant associated with the dry simulated conditions, the spatial variation in emissivity arises because the reflectivity/emissivity depends on the local incidence angle [(9) and (10)]. Since the fluvial erosion domain exhibits significantly more variation in brightness temperature than the diffusive erosion domain, despite relatively similar ranges in soil temperatures between the two domains, it follows that the range in emissivity is larger in the fluvial erosion domain. This suggests that the hillslope-scale organization of emissivity is sensitive to topographic ruggedness, an important implication for formulation of soil moisture retrieval algorithms. Several retrieval algorithms (e.g., [10] and [63]) approximate emissivity as the brightness temperature normalized by an independently measured or estimated soil surface temperature (T_{bp}/T_S), which holds to equality if f_c in (1) equals 0. The scattering terms in the RTM shown in (1) (T_C, f_c, ω_p, and τ_p) exert greater influence on T_{bp} as e_p decreases. Hence, although simulated vegetation biomass is low in this modeling study, vegetation scattering may degrade the accuracy of an approximate value of emissivity in areas of the landscape in which incidence angles are high due to the relative positioning of the hillslope and observing satellite. The effects of topography on the spatial distribution of emissivity differ, depending on the wetness conditions. For the relatively dry and spatially invariant conditions modeled in this study, the principal effect of topography on the spatial distribution of emissivity is through the dependence of emissivity on local incidence angle as expressed in (9) and (10). Similarly, control of local incidence angles is also the primary topographic effect on emissivity under exceptionally wet conditions associated with almost uniformly saturated near-surface soil moisture conditions. However, at intermediate wetness and particularly during the dry-down phase of the hydrologic cycle, the hillslope-scale distribution of emissivity is influenced by topography in the following two ways: 1) by the spatial distribution of the dielectric constant, which reflects the physical processes responsible for moisture redistribution in the subsurface, and 2) by the spatial distribution of local incidence angle as controlled by the distribution of topographic slope and aspect.

To diagnose the relative impacts of spatial variability in surface states input to the RTM for the assumed sensor sky position, we recompute T_{bh} and T_{bv} at each computation node using the locally derived value of θ and φ, but with the spatially averaged values of T_S, T_C, f_c, m_v, LAI, and h reported in Table I. The maps of T_{bh} and T_{bv} computed with spatially averaged RTM inputs are denoted as T_{bh}^{sa} and T_{bv}^{sa}, respectively. Denoting the brightness temperatures in both polarizations computed from spatially distributed RTM inputs (i.e., those presented in Fig. 5) as T_{bh}^{sv} and T_{bh}^{sv}, respectively, Fig. 6 shows the impact of hillslope-scale heterogeneity in surface states on hillslope-scale microwave radiation emission [i.e., $(T_{bh}^{sv} - T_{bh}^{sa})$ and $(T_{bv}^{sv} - T_{bv}^{sa})$]. In the diffusive erosion domain, the impact of spatial heterogeneity in the surface states results in values of $(T_{bh}^{sv} - T_{bh}^{sa})$ ranging from approximately -5.4 to $+2.3$ K [Fig. 6(a)], while in the fluvial erosion domain, spatial heterogeneity leads to values of $(T_{bh}^{sv} - T_{bh}^{sa})$ ranging from -25.0 to $+5.5$ K [Fig. 6(c)]. West- and north-facing pixels exhibit the lowest values of $(T_{bh}^{sv} - T_{bh}^{sa})$ in both domains, while in the fluvial erosion domain, west-facing pixels demonstrate the lowest values of $(T_{bh}^{sv} - T_{bh}^{sa})$. Conversely, south- and southeast-facing pixels demonstrate the highest values of $(T_{bh}^{sv} - T_{bh}^{sa})$ in both the diffusive and fluvial erosion domains. Values of $(T_{bv}^{sv} - T_{bv}^{sa})$ range from approximately -5.7 to $+2.4$ K in the diffusive erosion domain [Fig. 6(b)] and approximately -25.5 to $+5.5$ K in the fluvial erosion domain [Fig. 6(d)]. Pixels with aspects ranging west to north demonstrate the lowest values of $(T_{bv}^{sv} - T_{bv}^{sa})$ in the respective domains. In the fluvial erosion domain a few north-facing pixels (primarily clustered around pixels with $\theta \geq 90^\circ$) exhibit positive values of $(T_{bv}^{sv} - T_{bv}^{sa})$, suggesting that such pixels possess high θ associated with T_{bv} that increases with higher m_v, and lower T_S and T_C that predominate in these areas. It is important to note that for this particular set of experiments, the spatial patterns in $(T_{bh}^{sv} - T_{bh}^{sa})$ and $(T_{bv}^{sv} - T_{bv}^{sa})$ in Fig. 6 likely arise due mostly to spatial variation in soil and canopy temperature rather than soil moisture and optical thickness. For the simulated conditions, near-surface soil moisture is relatively low, and LAI ranges from approximately 0.6 to 0.9.

B. Sensitivity of Aggregate Brightness Temperature to Satellite Sky Position

In Section III-A, we demonstrate that microwave brightness temperature varies significantly at hillslope scales due to the effects of topography on both the spatial organization of surface states as well as angles describing the observational geometry. Here, we assess the sensitivity of spatially aggregated brightness temperature to satellite azimuth angle (ζ_S) to diagnose the potential effects of topography at the sensor.

The spatial distribution of horizontally and vertically polarized microwave brightness temperatures was computed through the RTM using the previously described instantaneous surface states evolved by tRIBS–VEGGIE for both computational domains. In this portion of this paper, we assume the satellite viewing angle (δ_S) is 40° and allow the azimuth angle to the satellite (ζ_S) to vary from 1° to 360°, in ζ_S increments of 1°. For each domain, this yields 360 spatial maps of horizontally and vertically polarized brightness temperature derived from spatially distributed land surface states, which are denoted as T_{bh}^{sv} and T_{bv}^{sv}, respectively. Each of these hillslope-scale brightness temperature maps are spatially aggregated, weighing each pixel according to its contribution to the radiation received at the sensor. The contribution of a pixel to the bulk microwave radiation observed at the sensor depends on the solid angle $\Omega = A\cos\theta/r^2$, where A is the surface area of the pixel, and r is the distance from the pixel to the radiometer antenna [19]. Given the relatively small domain size, r does not vary substantially within the domains considered in this paper

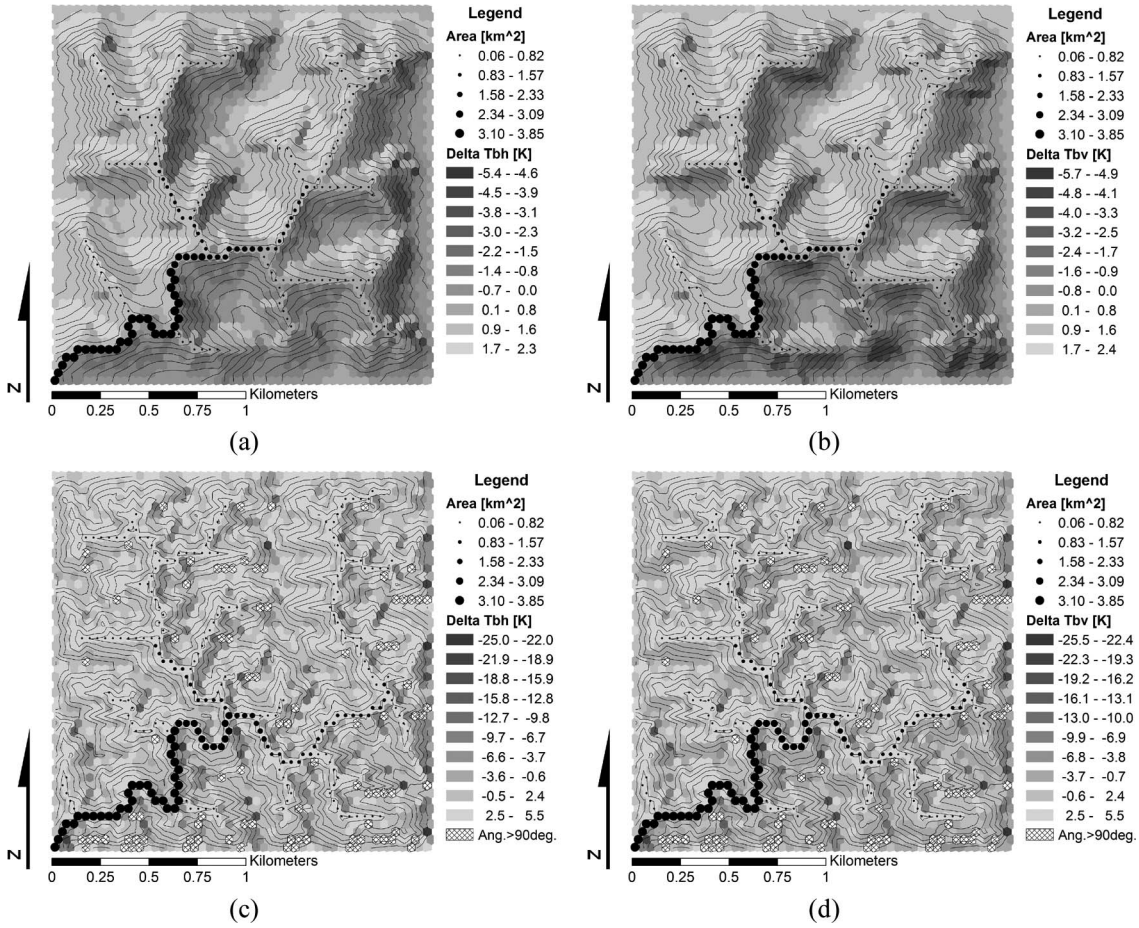

Fig. 6. Spatial distribution of difference between simulated brightness temperatures using spatially varied and spatially averaged surface states, assuming $\zeta_S = 150^\circ$ and $\delta_S = 40^\circ$ for (a) diffusive erosion terrain in the horizontal polarization, (b) diffusive erosion terrain in the vertical polarization, (c) fluvial erosion terrain in the horizontal polarization, and (d) fluvial erosion terrain in the vertical polarization. Note that brightness temperatures in (c) and (d) are plotted in geometric intervals due to the large range of variability.

and is assumed uniform. Therefore, in ζ_S increments of 1°, the horizontally and vertically polarized microwave brightness temperature observed at the sensor ($\overline{T}_{bh}^{sv}$ and $\overline{T}_{bv}^{sv}$, respectively) due to emission from the visible pixels within the domain can be computed as

$$\overline{T}_{bp}^{sv} = \frac{\sum_{j=1}^{n} T_{bp,j}^{sv} \Omega_j}{\sum_{j=1}^{n} \Omega_j} \tag{12}$$

where n is the number of pixels visible at given satellite azimuth (ζ_S).

For comparison purposes, we consider two cases in which brightness temperatures at the sensor are modeled, assuming that m_v, T_S, T_C, and LAI are spatially uniform and equal to the mean value illustrated in Table I for each domain. The following two cases are meant to capture potentially important hypothetical microwave emission modeling scenarios within a consistent land surface modeling environment: 1) a coarse-scale land surface model augmented with high-resolution (e.g., 30 m) digital elevation data to encompass topographic effects on observational geometry and 2) a coarse-scale land surface model neglecting topographic effects on observational geometry. In the first case, topographic effects on θ and φ are included in modeling the dependence of horizontally and vertically polarized brightness temperature at the sensor on ζ_S. These brightness temperatures modeled at the sensor are denoted as $\overline{T}_{bh}^{sa}$ and $\overline{T}_{bv}^{sa}$, respectively, and are computed by substituting T_{bp}^{sa} for T_{bp}^{sv} in the summation on the right-hand side of (12). In the second case, topographic effects are neglected, and we assume that $\theta = \delta_S = 40^\circ$. We denote the modeled brightness temperatures at the sensor, which does not vary with satellite azimuth (ζ_S), as $\overline{T}_{bh,\mathrm{flat}}$ and $\overline{T}_{bv,\mathrm{flat}}$ in the latter case.

For the diffusive erosion domain (e.g., rolling hills with relatively shallow slopes), $\overline{T}_{bh}^{sv}$, $\overline{T}_{bh}^{sa}$, $\overline{T}_{bv}^{sv}$, and $\overline{T}_{bv}^{sa}$ vary in a sinusoidal fashion with azimuth angle to the satellite (ζ_S) [Fig. 7(a) and (b)]. This sinusoidal variation brightness temperature modeled at the sensor with ζ_S arises because the assumed value of $\delta_S(40^\circ)$ is greater than the maximum slope in the domain. For any value of ζ_S, this leads to a distribution of θ within the diffusive erosion domain that leads to the inclusion of every computational node in aggregation of the pixel-scale brightness temperatures. This contrasts with the results from the fluvial erosion landscape (e.g., rugged hills with relatively steep slopes), which exhibits a more variable relationship between aggregated brightness temperatures and ζ_S [Fig. 7(c) and (d)]. Because the value of δ_S equal to 40° is less than the maximum

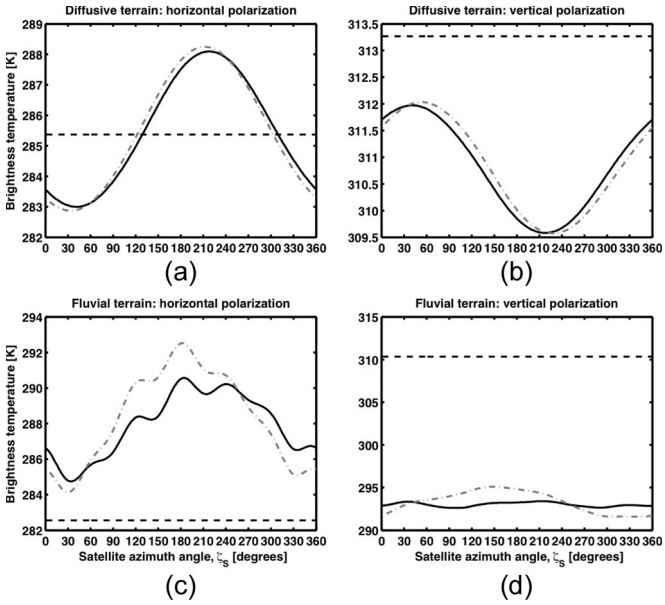

Fig. 7. Spatial mean values of brightness temperatures as a function of satellite azimuth angle for (a) diffusion-dominated terrain in the horizontal polarization, (b) diffusion-dominated terrain in the vertical polarization, (c) fluvial-erosion-dominated terrain in the horizontal polarization, and (d) fluvial-erosion-dominated terrain in the vertical polarization. The gray dashed–dotted line represents $\overline{T}_{bh}^{sv}$ and $\overline{T}_{bv}^{sv}$, the solid black line represents $\overline{T}_{bh}^{sa}$ and $\overline{T}_{bv}^{sa}$, and the black dashed line represents $\overline{T}_{bh,\mathrm{flat}}$ and $\overline{T}_{bv,\mathrm{flat}}$.

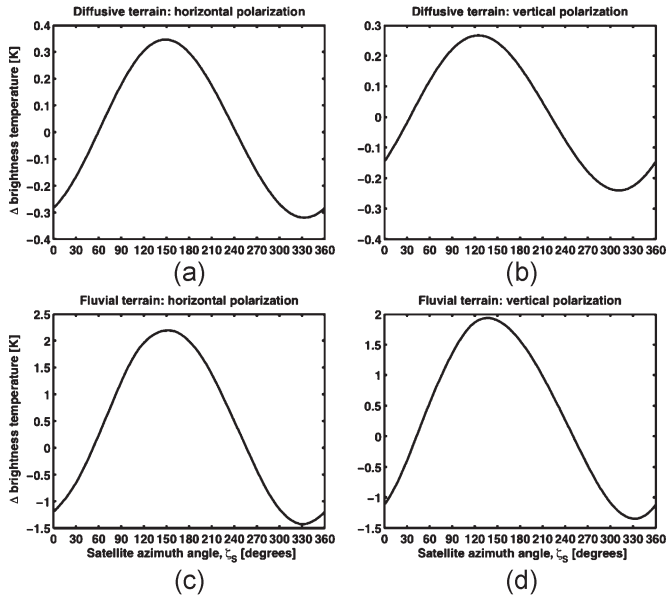

Fig. 8. $(\overline{T}_{bp}^{sv} - \overline{T}_{bp}^{sa})$ as a function of satellite azimuth angle (ζ_S) for (a) diffusion-dominated terrain in the horizontal polarization, (b) diffusion-dominated terrain in the vertical polarization, (c) fluvial-erosion-dominated terrain in the horizontal polarization, and (d) fluvial-erosion-dominated terrain in the vertical polarization.

slope in the fluvial erosion domain, groups of pixels depending on ζ_S will exhibit θ greater than or equal to the upper 90° limit. At any value of ζ_S, those pixels with $\theta \geq 90°$ are not included in aggregation of pixel-scale brightness temperatures because they cannot be observed by the sensor.

Another important contrast between the diffusive and fluvial erosion terrains lies in the amplitude of variability in aggregated brightness temperatures with ζ_S. In the horizontal polarization, $\overline{T}_{bh}^{sv}$ varies from a low of about 283 K at ζ_S of approximately 40° to a maximum of approximately 288 K at approximately ζ_S equal to 220°, which is a range of 5 K in the diffusive erosion landscape [Fig. 7(a)]. In the fluvial erosion domain, $\overline{T}_{bh}^{sv}$ ranges from a low of around 284 K at ζ_S equal to approximately 40° to a maximum of approximately 292 K at ζ_S equal to 180°, which gives an amplitude of about 8 K for conditions of spatially varying surface states [Fig. 7(c)]. In comparison, the corresponding amplitude of variation $\overline{T}_{bh}^{sa}$ is approximately 5 K [Fig. 7(c)]. The impact of spatial heterogeneity in surface states, as illustrated in the more rugged domain by the difference between $\overline{T}_{bh}^{sv}$ and $\overline{T}_{bh}^{sa}$ [Fig. 7(c)] is close to the sensitivity of the radiometer for many values of ζ_S and greater than the sensitivity of many operational and planned microwave radiometers at a few particular values of ζ_S [3], [4].

The $\overline{T}_{bv}^{sv}$ in the diffusive erosion landscape exhibits a maximum of about 312 K at ζ_S equal to approximately 40° and a minimum slightly higher than 309.5 K at ζ_S equal to about 220°, corresponding to a range in aggregated $\overline{T}_{bv}^{sv}$ of approximately 2.5 K [Fig. 7(b)]. By comparison, $\overline{T}_{bv}^{sv}$ in the fluvial erosion domain exhibits a range of approximately 3 K (slightly greater than the radiometer sensitivity), with an approximate minimum of 292 K at ζ_S near 330° and an approximate maximum of 295 K at near 150° [Fig. 7(d)].

Comparing the modeled brightness temperatures at the sensor that include topographic effects on incidence angle and polarization rotation ($\overline{T}_{bh}^{sv}$ and $\overline{T}_{bh}^{sa}$) to the modeled brightness temperatures that neglect topographic effects on incidence angle and polarization rotation, $\overline{T}_{bh,\mathrm{flat}}$ is approximately 285.5 K in the rolling topographic domain [Fig. 7(a)] and 282.5 K in the rugged topographic domain [Fig. 7(c)]. In the diffusive domain, the value of $\overline{T}_{bh,\mathrm{flat}}$ is approximately the midpoint of variation in $\overline{T}_{bh}^{sv}$ and $\overline{T}_{bh}^{sa}$ with ζ_S [Fig. 7(a)], while $\overline{T}_{bh,\mathrm{flat}}$ is at least 1.5 K less than the minimum values of $\overline{T}_{bh}^{sv}$ and $\overline{T}_{bh}^{sa}$ in the fluvial domain [Fig. 7(c)]. In the vertical polarization, $\overline{T}_{bv,\mathrm{flat}}$ is more than 1 K higher than the maximum values of $\overline{T}_{bv}^{sv}$ and $\overline{T}_{bv}^{sa}$ in the diffusive domain [Fig. 7(b)] and at least 15 K higher than the maximum value of $\overline{T}_{bv}^{sv}$ in the fluvial domain [Fig. 7(d)]. Fig. 7 depicts the following two important findings of this study: 1) the difference between $\overline{T}_{bp}^{sv}$ and $\overline{T}_{bp}^{sa}$ demonstrates the role of covariation in the land surface factors affecting microwave emission at hillslope scales in the modeled brightness temperature at the sensor and 2) the difference between $\overline{T}_{bp,\mathrm{flat}}$ and $\overline{T}_{bp}^{sa}$ illustrates the impact of hillslope-scale topography on modeled brightness temperature at the sensor vis-á-vis its influence on observational geometry.

The difference in modeled brightness temperatures observed at the sensor ($\overline{T}_{bh}^{sv} - \overline{T}_{bh}^{sa}$ and $\overline{T}_{bv}^{sv} - \overline{T}_{bv}^{sa}$) as a function of ζ_S is shown more clearly in Fig. 8, which illustrates the impact of hillslope-scale organization in factors affecting microwave energy emission at the observing sensor. In general, the fluvial domain [Fig. 7(c) and (d)] is more sensitive to hillslope-scale soil moisture, soil temperature, and vegetation variation than is the diffusive domain [Fig. 7(a) and (b)]. At ζ_S near 330°, $\overline{T}_{bh}^{sv}$ is approximately 0.3 K lower than $\overline{T}_{bh}^{sa}$ in the topographically smoother terrain [Fig. 8(a)], and $\overline{T}_{bh}^{sv}$ is approximately 1.5 K lower than aggregated $\overline{T}_{bh}^{sa}$ in the

more topographically rough terrain [Fig. 8(c)]. Conversely, when the satellite is situated to the south of the landscape (ζ_S near 150°), $\overline{T}_{bh}^{sv}$ is warmer than $\overline{T}_{bh}^{sa}$: approximately 0.3 and 2.0 K in the topographically smoother [Fig. 8(a)] and more rugged [Fig. 8(c)] domains, respectively. The ζ_S corresponding to the minimum and maximum values of $(\overline{T}_{bh}^{sv} - \overline{T}_{bh}^{sa})$ are accounted for by the hillslope-scale organization and correlation of soil moisture, soil temperature, and vegetation biomass. By contrast, $\overline{T}_{bv}^{sv}$ differs from $\overline{T}_{bv}^{sa}$ by at most about 0.25 K in the topographically smoother domain. The value of $(\overline{T}_{bv}^{sv} - \overline{T}_{bv}^{sa})$ is a maximum when at ζ_S near 130° and a minimum at ζ_S near 300°. Meanwhile, $\overline{T}_{bv}^{sv}$ is up to 2 K greater that and nearly 1.5 K lower than $\overline{T}_{bv}^{sa}$ in the more topographically rugged domain [Fig. 8(d)]. The nonsymmetry in Fig. 8(d) about 0 K and change of phase with respect to Fig. 8(b) is due to the fact that T_{bv} exhibits nonmonotonic dependence on θ when θ is greater than approximately 65°.

C. Effects of Hillslope-Scale Heterogeneity at the Scale of Planned and Existing Sensors

The influence of hillslope-scale topography on local incidence angle over real terrain is also studied. The case considered is a 43 km × 59 km area within north-central New Mexico, which contains the Sevilleta National Wildlife Refuge and Long-Term Ecological Research station. The DEM was obtained from the Sevilleta Spatial Database (see http://sevilleta.unm.edu/data/archive/gis/) derived from interferometric synthetic aperture radar at a resolution of 10 m. Elevation within the area ranges from 1403 to 2802 m mean sea level.

Local incidence angle (θ) is computed through (4) at every DEM cell within imposed 10, 25, and 40 km windows meant to represent the size of a single radiometer pixel based on the topographic slope (α_∇) and aspect (ζ_∇) at each DEM cell and assuming $\zeta_S = 150°$ and $\delta_S = 40°$. This is a simplifying assumption, which could be relaxed by computing ζ_S and δ_S at each DEM pixel, knowing the location of the subsatellite point on the Earth's surface and the orbital altitude of the sensor. We then compute the empirical histograms of local incidence angle within each of the three area aggregations.

The empirical histograms shown in Fig. 9 illustrate that for each area aggregation, both slope and aspect control the distribution of incidence angle. The influence of aspect on the histograms is reflected on frequency peaks in Fig. 8. Undoubtedly, the fact that there are four peaks in the histogram of θ arises because aspect angle (cardinal direction of maximum gradient) can take only eight values on a rectangular grid. However, the presence of a coherent topographic structure in any study domain (such as the north–south-oriented ridges present in the study areas) will lead to distinct ranges of incidence angles that are encountered more frequently, irrespective of the terrain model (i.e., regular grid spacing versus irregular mesh). The frequency at which particular ranges of incidence angles are encountered within the area aggregation does not change substantially with increasing spatial aggregation (Fig. 9). The fact that the histograms of incidence angles seen in Fig. 9 do not change substantially as the domain size is increased

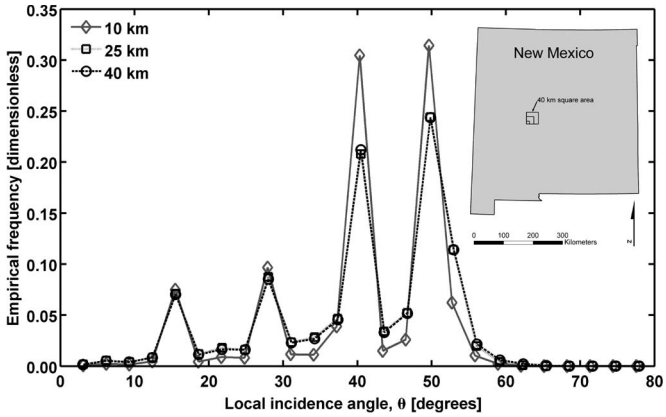

Fig. 9. Empirical frequency distributions of local incidence angles computed from a 10-m digital elevation model for square domains of size 10 km (solid line marked by open diamonds), 25 km (dotted line marked by open squares), and 40 km (dashed line marked by open circles), assuming a satellite azimuth angle of 150° and a zenith angle of 40°.

suggests that the results of the synthetic experiments presented in this paper are likely qualitatively informative for footprint scales of planned and existing satellite radiometers. Together, Figs. 7–9 suggest that the magnitude of the brightness temperature sensitivity to satellite viewing position, however, is likely a function of both the overall relief (difference in maximum and minimum elevation), as well as the topographic ruggedness (distribution of slopes and hillslope lengths) within the satellite footprint.

IV. Implications and Conclusion

In summary, on an individual hillslope, topography affects the amount of solar radiation received, therefore impacting local soil moisture conditions, temperature conditions, and dominant vegetation. Moreover, the topographic patterns in soil moisture and incoming solar radiation induce correlated patterns in vegetation biomass, water content, and height [26]–[28], which enhances topographic contrasts in the surface states that control emission of microwave radiation. Hillslope-scale topography also controls the incidence angle and polarization rotation required to capture topographic effects in modeling the microwave brightness temperature at the sensor. Significant variation in modeled hillslope-scale brightness temperatures is a result of variation in the following parameters: 1) soil moisture and temperature; 2) vegetation water content, height, and temperature; and 3) local incidence angle and polarization rotation associated with topography. At the sensor, modeled brightness temperatures are sensitive to the satellite azimuth angle and zenith angle because the histogram of hillslope-scale incidence angles reflects both the distribution of slopes and aspects within the observation area and the location of the satellite with respect to the observation area at the time of observation. The magnitude of this sensitivity is a function primarily of the degree of topographic ruggedness (or smoothness). For the synthetic domains in which we simulate brightness temperature, the fluvial erosion domain (e.g., rugged terrain with relatively steep slopes) exhibits more variability in both brightness temperatures modeled at hillslope scales and at

the sensor because shorter hillslopes and higher slope angles result in both small-scale variability in surface states and a wide range of local incidence angles. Spatial heterogeneity in the surface states input to the RTM considerably affects the spatial distribution of hillslope-scale brightness temperatures. Further, as Fig. 8 depicts, the impact of spatially heterogeneous surface states on modeled brightness temperatures at the sensor become progressively more pronounced as the terrain becomes steeper. In general, if the satellite zenith angle (δ_S) is less than the maximum slope angle of the area being observed, those pixels with slope angles (α_∇) greater than δ_S and slope aspects (ζ_∇) coaligned with ζ_S may not contribute to the observation because they possess $\theta \geq 90^\circ$. This impact can be seen in the dependence of $\overline{T}_{bh}^{sv}$ and $\overline{T}_{bv}^{sv}$ on ζ_S in the fluvial erosion landscape [Fig. 7(c) and (d)] and reflects the nonsymmetric nature of spatial variability in surface states with topography. For example, $\overline{T}_{bh}^{sv}$ is slightly more than 2 K greater than aggregate $\overline{T}_{bh}^{sa}$ at ζ_S approximately equal to 150° in the fluvial erosion setting, even with relatively dry conditions and little vegetation. At this ζ_S (with the satellite viewing the landscape from the southeast), south- and east-facing hillslopes with low m_v, high T_S, and high T_C would tend to enhance brightness temperature, while many north-facing hillslopes with high m_v, low T_S, and low T_C do not contribute to the predicted observation because they possess unfeasibly high values of θ. In general, when the value of ζ_S is such that the satellite is south (north) of the domain, (12) dictates that the brightness temperature modeled at the sensor ($\overline{T}_{bh}^{sv}$ and $\overline{T}_{bv}^{sv}$) will preferentially weight warmer (cooler) pixels because those pixels also possess lower θ. This implies that when modeling the microwave observation at the sensor, variation in the land surface state associated with hillslope-scale topography is progressively more important as the terrain modeled becomes steeper. This work is of potential importance for applications that require modeling surface microwave emission in areas of nonnegligible topographic variation. In particular, we discuss this work in the context of understanding how topography may lead to substantial error in retrieved soil moisture, disaggregation of radiometer products to hillslope scales, and assimilation of radiometer data into hydrologic models in topographically variable terrain.

As of now, there exist no spaceborne radiometer data with which to validate the findings of this work. A substantial body of work exists in formulation and validation of retrieval algorithms based on numerical inversion of (1) using simulated, airborne, or tower brightness temperature observations together with *in situ* soil moisture measurements (e.g., [2], [6], [7], and [64]). These works are confined, however, to relatively flat terrain, and in some cases, substantial error exists between retrieved and measured values of soil moisture. This paper attempts to discern, to the extent possible in a modeling framework without spaceborne L-band data for validation purposes, the amount of error at the sensor that can potentially be attributed to factors associated with topographic variation that are commonly neglected in emission modeling. The potential for large errors in retrieval algorithms in topographically variable terrain has been acknowledged in the design of the SMOS mission by Mialon *et al.* [22]. They outline a technique to flag SMOS pixels in which incidence angle effects associated with topography are sufficiently severe to render the retrieved soil moisture as either suspect (termed by the authors moderate topography) or unreliable (termed by the authors strong topography) by fitting a log-polynomial model to the semivariogram of DEMs. Together with an RTM, they use a single fitting parameter computed from the DEM to identify SMOS pixels in which the retrieval error due to topographic effects on incidence angle is likely to be near or greater than the required 4% accuracy of the SMOS satellite. Introducing aspect to their technique may better refine the location of pixels flagged, particularly in areas with spatially coherent topographic structures (e.g., the Alps and Pyrenees). In a study of synthetic landscapes, Sandells *et al.* [23] found that potential soil moisture retrieval errors using the algorithm outlined in [64] due to topographic effects on incidence angles may be small for relatively simple topographic geometries. Although they did not include aspect explicitly in their analysis of synthetic landscapes, they did note that portions of the landscape sloping away from the sensor are likely to introduce larger errors than portions of the landscape with identical ground slope but sloping toward the sensor. The potential impact of topographic ruggedness on approximating emissivity as T_{bp}/T_S mentioned above merits further investigation for formulating soil moisture retrieval algorithms in areas of substantial topographic variability. Variation in observed brightness temperature with satellite azimuth angle at coarse spatial scales, while potentially significant, can be dampened by normalizing with an accurate estimate or observation of the average soil temperature at the same scale. In sparsely vegetated regions with substantial topographic slopes, however, the nearly linear relationship between emissivity and T_{bp}/T_S can break down in areas where emissivity is low (because of high incidence angles). Errors in the approximate value of emissivity could be significant and will depend on the relative proportion of steep hillslopes within the landscape being observed. Until spaceborne L-band data become available, uncertainties in the degree to which topographic controls on viewing geometry and factors affecting emission from the surface contribute to error in retrieved moisture from actual brightness temperature measurements will remain an active area of research.

Disaggregation of soil moisture patterns retrieved from brightness temperature observations is an active area of research [65], [66]. Often, these disaggregation methods seek to provide a spatial distribution of soil moisture at sufficiently high resolution to initialize watershed hydrology models. Several of these efforts have posed disaggregation as a geostatistical interpolation based on ancillary data such as soils, vegetation, and topography [35], [66]–[68]. Given that the range of variation in modeled brightness temperature is finite and varies with incidence angle, our study suggests that histograms of incidence angle and polarization rotation derived from DEM analysis may be useful constrains to impose on these disaggregation frameworks. By bracketing the range of brightness temperature variation for a given observation, ancillary data such as soils maps, maps of normalized difference vegetation index or other temperature-dependent maps cab be used to narrow the hillslope-scale feasible range of soil moisture variability. A series of local optimization problems can then be solved to find the spatial distribution of soil moisture that satisfies these local

constraints imposed by analysis of DEMs and ancillary data while preserving the brightness temperature observed at the sensor. The forthcoming L-band SMOS satellite [3] represents an innovative approach to microwave soil moisture observation that may advance the ability to downscale brightness observations to hillslope scales. It incorporates a multiangular viewing concept that observes the brightness temperature of a particular location at two polarizations (vertical and horizontal) and viewing angles that range from 0° to 55° off-nadir. A consequence of this sensor configuration is that the spatial resolution of the brightness temperature products varies with viewing angle. However, since the sensor provides multiple observations over the same location over a period of time short enough to neglect the dynamics of soil moisture redistribution, the multiviewing angle observations of brightness temperature could potentially be used to provide multiple constraints on the range of local brightness temperature in efforts to disaggregate brightness temperatures to hillslope scales using the conceptual methodology outlined above.

Finally, this study is instructive for efforts to use microwave brightness data to update hydrological models through data assimilation. Many data assimilation frameworks such as the ensemble Kalman filter require the use of an observation operator that ingests information about the model state to produce predicted observations (e.g., see [11], [12], and [69]–[71]). Data assimilation is particularly attractive to constrain soil moisture estimates from watershed ecohydrology models such as tRIBS–VEGGIE to observational data [72]–[74] partly because soil moisture controls the partitioning of rainfall into infiltration and runoff as well as the partitioning of incoming radiation into latent and sensible heat. This paper highlights the potential importance in hillslope-scale soil moisture data assimilation studies of including topographic effects on local incidence angle and polarization rotation when the observation operator is an RTM. It also implies that to adequately capture these effects, the sky position of the satellite relative to the area being studied must be known when modeling the microwave brightness observation at the sensor.

ACKNOWLEDGMENT

The authors would like to thank three anonymous reviewers for their comments, which substantially improved the manuscript. A. N. Flores would like to thank R. Koster for graciously providing important comments to an earlier version of the manuscript.

REFERENCES

[1] E. Njoku and D. Entekhabi, "Passive microwave remote sensing of soil moisture," *J. Hydrol.*, vol. 184, no. 1/2, pp. 101–129, Oct. 1996.

[2] W. T. Crow, M. Drusch, and E. F. Wood, "An observation system simulation experiment for the impact of land surface heterogeneity on AMSR-E soil moisture retrieval," *IEEE Trans. Geosci. Remote Sens.*, vol. 38, no. 8, pp. 1622–1631, Aug. 2001.

[3] Y. H. Kerr, P. Waldteufel, J.-P. Wigneron, J.-M. Martinuzzi, J. Font, and M. Berger, "Soil moisture retrieval from space: The Soil Moisture and Ocean Salinity (SMOS) mission," *IEEE Trans. Geosci. Remote Sens.*, vol. 39, no. 8, pp. 1729–1735, Aug. 2001.

[4] D. Entekhabi, E. Njoku, P. Houser, M. Spencer, T. Doiron, J. Smith, R. Girard, S. Belair, W. Crow, T. Jackson, Y. Kerr, J. Kimball, R. Koster, K. McDonald, P. O'Neill, T. Pulz, S. Running, J. Shi, E. Wood, and J. van Zyl, "The Hydrosphere State (HYDROS) mission concept: An Earth system pathfinder for global mapping of soil moisture and land freeze/thaw," *IEEE Trans. Geosci. Remote Sens.*, vol. 42, no. 10, pp. 2184–2195, Oct. 2004.

[5] S. Paloscia, G. Macelloni, and E. Santi, "Soil moisture estimates from AMSR-E brightness temperatures by using a dual-frequency algorithm," *IEEE Trans. Geosci. Remote Sens.*, vol. 44, no. 11, pp. 3135–3144, Nov. 2006.

[6] J.-P. Wigneron, P. Waldteufel, A. Chanzy, J.-C. Calvet, and Y. Kerr, "Two-dimensional microwave interferometer retrieval capabilities over land surfaces (SMOS mission)," *Remote Sens. Environ.*, vol. 73, no. 3, pp. 270–282, Sep. 2000.

[7] T. Pellarin, J.-P. Wigneron, J.-C. Calvet, and P. Waldteufel, "Global soil moisture retrieval from a synthetic L-band brightness temperature data set," *J. Geophys. Res.*, vol. 108, no. D12, p. 4364, Jun. 2003.

[8] E. G. Njoku and J.-A. Kong, "Theory for passive microwave remote sensing of near-surface soil moisture," *J. Geophys. Res.*, vol. 82, no. 20, pp. 3108–3118, Jul. 1977.

[9] T. Mo, B. J. Choudhury, T. J. Schmugge, J. R. Wang, and T. J. Jackson, "A model for microwave emission from vegetation-covered fields," *J. Geophys. Res.*, vol. 97, no. C13, pp. 11 229–11 237, Dec. 1982.

[10] W. T. Crow, S. T. K. Chan, D. Entekhabi, P. R. Houser, A. Y. Hsu, T. J. Jackson, E. G. Njoku, P. E. O'Neill, J. Shi, and X. Zhan, "An observing system simulation experiment for hydros radiometer-only soil moisture products," *IEEE Trans. Geosci. Remote Sens.*, vol. 43, no. 6, pp. 1289–1303, Jun. 2005.

[11] S. A. Margulis, D. McLaughlin, D. Entekhabi, and S. Dunne, "Land data assimilation and estimation of soil moisture using measurements from the Southern Great Plains 1997 Field Experiment," *Water Resour. Res.*, vol. 38, no. 12, p. 1299, Dec. 2002.

[12] R. H. Reichle, D. B. McLaughlin, and D. Entekhabi, "Hydrologic data assimilation with the ensemble Kalman filter," *Mon. Weather Rev.*, vol. 130, no. 1, pp. 103–114, Jan. 2002.

[13] T. Pellarin, Y. Kerr, and J.-P. Wigneron, "Global simulation of brightness temperatures at 6.6 and 10.7 GHz over land based on SMMR data set analysis," *IEEE Trans. Geosci. Remote Sens.*, vol. 44, no. 9, pp. 2492–2505, Sep. 2006.

[14] T. Holmes, M. Drusch, J.-P. Wigneron, and R. de Jeu, "A global simulation of microwave emission: Error structures based on output from ECMWF's operational integrated forecast system," *IEEE Trans. Geosci. Remote Sens.*, vol. 46, no. 3, pp. 846–856, Mar. 2008.

[15] I. Rodríguez-Iturbe, G. K. Vogel, R. Rigon, D. Entekhabi, F. Castelli, and A. Rinaldo, "On the spatial organization of soil moisture fields," *Geophys. Res. Lett.*, vol. 22, no. 20, pp. 2757–2760, 1995.

[16] T. J. Schmugge and T. J. Jackson, "Soil moisture variability," in *Scaling Up in Hydrology Using Remote Sensing*, J. B. Stewart, E. T. Engman, R. A. Feddes, and Y. Kerr, Eds. New York: Wiley, 1996, pp. 183–192.

[17] R. Haverkamp, J.-Y. Parlange, R. Cuenca, P. J. Ross, and T. S. Steenhuis, "Scaling of the Richards equation and its application to watershed modeling," in *Scale Dependence and Scale Invariance in Hydrology*, G. Esposito, Ed. Cambridge, U.K.: Cambridge Univ. Press, 1998, pp. 190–223.

[18] A. W. Western, R. B. Grayson, G. Blöschl, G. R. Willgoose, and T. A. McMahon, "Observed spatial organization of soil moisture and its relation to terrain indices," *Water Resour. Res.*, vol. 35, no. 3, pp. 797–810, 1999.

[19] C. Mätzler and A. Standley, "Technical note: Relief effects for passive microwave remote sensing," *Int. J. Remote Sens.*, vol. 21, no. 12, pp. 2403–2412, 2000.

[20] Y. Kerr, F. Secherre, J. Lastenet, and J.-P. Wigneron, "SMOS: Analysis of perturbing effects over land surfaces," in *Proc. IGARSS*, Jul. 21–25, 2003, vol. 2, pp. 908–910.

[21] M. Talone, A. Camps, A. Monerris, M. Vall-Ilossera, P. Ferrazzoli, and M. Piles, "Surface topography and mixed-pixel effects on the simulated L-band brightness temperatures," *IEEE Trans. Geosci. Remote Sens.*, vol. 45, no. 7, pp. 1996–2003, Jul. 2007.

[22] A. Mialon, L. Coret, Y. H. Kerr, F. Secherre, and J.-P. Wigneron, "Flagging the topographic impact on the SMOS signal," *IEEE Trans. Geosci. Remote Sens.*, vol. 46, no. 3, pp. 689–694, Mar. 2008.

[23] M. J. Sandells, I. J. Davenport, and R. J. Gurney, "Passive L-band microwave soil moisture retrieval error arising from topography in otherwise uniform scenes," *Adv. Water Resour.*, vol. 31, no. 11, pp. 1433–1443, Nov. 2008.

[24] V. Y. Ivanov, E. R. Vivoni, R. L. Bras, and D. Entekhabi, "Catchment hydrologic response with a fully distributed triangulated irregular network model," *Water Resour. Res.*, vol. 40, no. 11, p. W11 102, Nov. 2004.

[25] V. Y. Ivanov, E. R. Vivoni, R. Bras, and D. Entekhabi, "Preserving high-resolution surface and rainfall data in operational-scale basin hydrology: A fully-distributed physically-based approach," *J. Hydrol.*, vol. 298, no. 1–4, pp. 80–111, Oct. 2004.

[26] V. Y. Ivanov, R. L. Bras, and E. R. Vivoni, "Vegetation-hydrology dynamics in complex terrain of semiarid areas—Part 1: A mechanistic approach to modeling dynamic feedbacks," *Water Resour. Res.*, vol. 44, p. W03 429, Mar. 2008.

[27] V. Y. Ivanov, R. L. Bras, and E. R. Vivoni, "Vegetation-hydrology dynamics in complex terrain of semiarid areas—Part 2: Energy-water controls of vegetation spatiotemporal dynamics and topographic niches of favorability," *Water Resour. Res.*, vol. 44, p. W03 430, Mar. 2008.

[28] V. Ivanov, R. L. Bras, and D. C. Curtis, "A weather generator for hydrological, ecological, and agricultural applications," *Water Resour. Res.*, vol. 43, p. W10 406, Oct. 2007.

[29] Y. H. Kerr and J.-P. Wigneron, "Vegetation models and observations—A review," in *Passive Microwave Remote Sensing of Land–Atmosphere Interactions*, B. Choudhury, Y. Kerr, E. Njoku, and P. Pampaloni, Eds. Utrecht, The Netherlands: VSP Publ., 1995.

[30] K. P. Kirdiashev, A. A. Chukhlansev, and A. M. Shutko, "Microwave radiation of the Earth's surface in the presence of vegetation," *Radio Eng. Electron. (USSR)*, vol. 24, pp. 256–264, 1979.

[31] U. Wegmuller, C. Matzler, and E. Njoku, "Canopy opacity models," in *Passive Microwave Remote Sensing of Land–Atmosphere Interactions*, B. J. Choudhury, Y. H. Kerr, E. G. Njoku, and P. Pampaloni, Eds. Utrecht, The Netherlands: VSP Publ., 1995, pp. 375–388.

[32] T. J. Jackson and T. J. Schmugge, "Vegetation effects on the microwave emission from soils," *Remote Sens. Environ.*, vol. 36, no. 3, pp. 203–212, Jun. 1991.

[33] A. A. V. de Griend and J.-P. Wigneron, "The b-factor as a function of frequency and canopy type at H-polarization," *IEEE Trans. Geosci. Remote Sens.*, vol. 42, no. 1, pp. 1–10, Jan. 2004.

[34] P. de Rosnay, J.-C. Calvet, Y. Kerr, J.-P. Wigneron, F. Lemaître, M. J. Escorihuela, J. M. Sabater, K. Saleh, J. Barrié, G. Bouhours, L. Coret, G. Cherela, G. Dedieu, R. Durbe, N. E. D. Fritz, F. Froissard, J. Hoedjes, A. Kruszewski, F. Lavenu, D. Suquia, and P. Waldteufel, "SMOSREX: A long term field campaign experiment for soil moisture and land surface process remote sensing," *Remote Sens. Environ.*, vol. 102, no. 3/4, pp. 377–389, Jun. 2006.

[35] O. Merlin, A. G. Chehbouni, Y. H. Kerr, E. G. Njoku, and D. Entekhabi, "A combined modeling and multispectral/multiresolution remote sensing approach for disaggregation of surface soil moisture: Application to SMOS configuration," *IEEE Trans. Geosci. Remote Sens.*, vol. 43, no. 9, pp. 2036–2050, Sep. 2005.

[36] M. Vall-Ilossera, A. Camps, I. Corbella, F. Torres, N. Duffo, A. Monerris, R. Sabia, D. Selva, C. Antolín, E. López-Baeza, J. F. Ferrer, and K. Saleh, "SMOS REFLEX 2003: L-band emissivity characterization of vineyards," *IEEE Trans. Geosci. Remote Sens.*, vol. 43, no. 5, pp. 973–982, May 2005.

[37] M. Schwank, C. Mätzler, M. Guglielmetti, and H. Flühler, "L-band radiometer measurements of soil water under growing clover grass," *IEEE Trans. Geosci. Remote Sens.*, vol. 43, no. 10, pp. 2225–2237, Oct. 2005.

[38] M. Guglielmetti, M. Schwank, C. Matzler, C. Oberdorster, J. Vanderborght, and H. Fluhler, "FOSMEX: Forest soil moisture experiments with microwave radiometry," *IEEE Trans. Geosci. Remote Sens.*, vol. 46, no. 3, pp. 727–735, Mar. 2008.

[39] J. A. Kong, *Electromagnetic Wave Theory*, 2nd ed. New York: Wiley-Interscience, 1990.

[40] M. C. Dobson, F. T. Ulaby, M. T. Hallikainen, and M. A. El-Rayes, "Microwave dielectric behavior of wet soil—Part II: Dielectric mixing models," *IEEE Trans. Geosci. Remote Sens.*, vol. GRS-23, no. 1, pp. 35–46, Jan. 1985.

[41] N. R. Peplinski, F. T. Ulaby, and M. C. Dobson, "Dielectric properties of soils in the 0.3–1.3 GHz range," *IEEE Trans. Geosci. Remote Sens.*, vol. 33, no. 3, pp. 803–807, May 1995.

[42] S. P. Friedman, "A saturation degree-dependent composite spheres model for describing the effective dielectric constant of unsaturated porous media," *Water Resour. Res.*, vol. 34, no. 11, pp. 2949–2961, Nov. 1998.

[43] M. A. Hilhorst, C. Dirksen, F. W. H. Kampers, and R. A. Feddes, "New dielectric mixture equation for porous materials based on depolarization factors," *Soil Sci. Soc. Amer. J.*, vol. 64, no. 5, pp. 1581–1587, 2000.

[44] V. L. Mironov, M. C. Dobson, V. H. Kaupp, S. A. Komarov, and V. N. Kleshchenko, "Generalized refractive mixing dielectric model for moist soils," *IEEE Trans. Geosci. Remote Sens.*, vol. 42, no. 4, pp. 773–785, Apr. 2004.

[45] G. C. Topp, J. L. Davis, and A. P. Annan, "Electromagnetic determination of soil water content: Measurements in coaxial transmission lines," *Water Resour. Res.*, vol. 16, no. 3, pp. 574–582, 1980.

[46] E. R. Vivoni, V. Y. Ivanov, R. L. Bras, and D. Entekhabi, "Generation of triangulated irregular networks based on hydrological similarity," *J. Hydrol. Eng.*, vol. 27, no. 4, pp. 959–973, Jul./Aug. 2004.

[47] R. H. Brooks and A. T. Corey, "Hydraulic properties of porous media," Colorado State Univ., Fort Collins, CO, Hydrol. Paper 3, 1964.

[48] G. B. Bonan, S. Levis, L. Kergoat, and K. W. Oleson, "Landscapes as patches of plant functional types: An integrating concept for climate and ecosystem models," *Glob. Biogeochem. Cycles*, vol. 16, no. 2, p. 1021, May 2002.

[49] X. Liang, D. P. Lettenmaier, E. F. Wood, and S. J. Burges, "A simple hydrologically based model of land surface water and energy fluxes for GCMs," *J. Geophys. Res.*, vol. 99, no. D7, pp. 14 415–14 428, Jul. 1994.

[50] F. Chen, K. Mitchell, J. Schaake, Y. Xue, H. Pan, V. Koren, Y. Duan, M. Ek, and A. Betts, "Modeling of land surface evaporation by four schemes and comparison with FIFE observations," *J. Geophys. Res.*, vol. 101, no. D3, pp. 7251–7268, 1996.

[51] R. D. Koster and M. J. Suarez, "Energy and water balance calculations in the MOSAIC LSM," Nat. Aerosp. Space Admin., Washington DC, NASA Tech. Memo. 104606, 1996. 9.

[52] C. D. Peters-Lidard, M. S. Zion, and E. F. Wood, "A soil–vegetation–atmosphere transfer scheme for modeling spatially variable water and energy balance processes," *J. Geophys. Res.*, vol. 102, no. D4, pp. 4303–4324, 1997.

[53] K. W. Oleson, G.-Y. Niu, Z. L. Yang, D. M. Lawrence, P. E. Thornton, P. J. Lawrence, R. Stockli, R. E. Dickinson, G. B. Bonan, and S. Levis, *Technical description of the Community Land Model (CLM)*. Boulder, CO: Nat. Center Atmos. Res., 2004.

[54] G. B. Bonan, "Land–atmosphere interactions for climate system models: Coupling biophysical, biogeochemical, and ecosystem dynamical processes," *Remote Sens. Environ.*, vol. 51, no. 1, pp. 57–73, Jan. 1995.

[55] G. B. Bonan, "A land surface model (LSM version 1.0) for ecological, hydrological, and atmospheric studies: Technical description and user's guide," Nat. Center Atmos. Res., Boulder, CO, NCAR Tech. Note NCAR/TN-417, 1996.

[56] P. J. Sellers, S. O. Los, C. J. Tucker, C. O. Justice, D. A. Dazlich, G. J. Collatz, and D. A. Randall, "A revised land surface parameterization (SiB2) for atmospheric GCMs—Part 2: The generation of global fields of terrestrial biophysical parameters from satellite data," *J. Clim.*, vol. 9, no. 4, pp. 706–737, 1996.

[57] S. Levis, G. B. Bonan, M. Vertenstein, and K. W. Oleson, "The Community Land Model's Dynamic Global Vegetation Model (CLMDGVM): Technical description and user's guide," Nat. Center Atmos. Res., Boulder, CO, NCAR Tech. Note NCAR/TN-459+IA, 2004.

[58] V. K. Arora and G. J. Boer, "A parameterization of leaf phenology for the terrestrial ecosystem component of climate models," *Glob. Change Biol.*, vol. 11, no. 1, pp. 39–59, Jan. 2005.

[59] T. G. Farr, P. A. Rosen, E. Caro, R. Crippen, R. Duren, S. Hensley, M. Kobrick, M. Paller, E. Rodriguez, L. Roth, D. Seal, S. Shaffer, J. Shimada, J. Umland, M. Werner, M. Oskin, D. Burbank, and D. Alsdorf, "The shuttle radar topography mission," *Rev. Geophys.*, vol. 45, p. RG2 004, May 2007.

[60] G. E. Tucker and R. L. Bras, "Hillslope processes, drainage density, and landscape morphology," *Water Resour. Res.*, vol. 34, no. 10, pp. 2751–2764, 1998.

[61] G. E. Tucker, S. T. Lancaster, N. M. Gasparini, R. L. Bras, and S. Rybarczyk, "An object-oriented framework for distributed hydrologic and geomorphic modeling using triangulated irregular networks," *Comput. Geosci.*, vol. 27, no. 8, pp. 959–973, Oct. 2001.

[62] G. E. Tucker, S. T. Lancaster, N. M. Gasparini, and R. L. Bras, "The Channel-Hillslope Integrated Landscape Development (CHILD) model," in *Landscape Erosion and Evolution Modelling*, R. Harmon and W. W. Doe, III, Eds. Norwell, MA: Kluwer, 2001.

[63] T. J. Jackson, "Measuring surface soil moisture using passive microwave remote sensing," *Hydrol. Process.*, vol. 7, no. 2, pp. 139–152, Jul. 1993.

[64] I. J. Davenport, J. Fernandez-Galvez, and R. J. Gurney, "A sensitivity analysis of soil moisture retrieval from the tau–omega microwave emission model," *IEEE Trans. Geosci. Remote Sens.*, vol. 43, no. 6, pp. 1304–1316, Jun. 2005.

[65] W. T. Crow and E. F. Wood, "The value of coarse-scale soil moisture observations for regional surface energy balance modeling," *J. Hydrometeorol.*, vol. 3, no. 4, pp. 467–482, Aug. 2002.

[66] G. Kim and A. P. Barros, "Downscaling of remotely sensed soil moisture with a modified fractal interpolation method using contraction mapping

and ancillary data," *Remote Sens. Environ.*, vol. 83, no. 3, pp. 400–413, Dec. 2002.
[67] N. S. Chauhan, S. Miller, and P. Ardanuy, "Spaceborne soil moisture estimation at high resolution: A microwave-optical/IR synergistic approach," *Int. J. Remote Sens.*, vol. 24, no. 22, pp. 4599–4622, 2003.
[68] J. Pellenq, J. Kalma, G. Boulet, G.-M. Saulnier, S. Wooldridge, Y. Kerr, and A. Chehbouni, "A disaggregation scheme for soil moisture based on topography and soil depth," *J. Hydrol.*, vol. 276, no. 1–4, pp. 112–127, May 2003.
[69] J. F. Galantowicz, D. Entekhabi, and E. G. Njoku, "Tests of sequential data assimilation retrieving profile soil moisture and temperature from observed L-band radiobrightness," *IEEE Trans. Geosci. Remote Sens.*, vol. 37, no. 4, pp. 1860–1870, Jul. 1999.
[70] S. Dunne and D. Entekhabi, "An ensemble-based reanalysis approach to land data assimilation," *Water Resour. Res.*, vol. 41, no. 2, p. W02 013, Feb. 2005.
[71] S. Dunne and D. Entekhabi, "Land surface state and flux estimation using the ensemble Kalman smoother during the Southern Great Plains 1997 Field Experiment," *Water Resour. Res.*, vol. 42, no. 1, p. W01 407, Jan. 2006.
[72] E. E. van Loon and P. A. Troch, "Tikhonov regularization as a tool for assimilating soil moisture data in distributed hydrological models," *Hydrol. Process.*, vol. 16, no. 2, pp. 531–536, Jan. 2002.
[73] N. N. Das and B. P. Mohanty, "Root zone soil moisture assessment using remote sensing and vadose zone modeling," *Vadose Zone J.*, vol. 5, pp. 296–307, Mar. 2006.
[74] S. Kim, Y. Tachikawa, and K. Takara, "Applying a recursive update algorithm to a distributed hydrologic model," *J. Hydrol. Eng.*, vol. 12, no. 3, pp. 336–344, May/Jun. 2007.

Alejandro N. Flores (S'08–M'09) received the B.S. and M.S. degrees in civil engineering from Colorado State University, Fort Collins, in 2001 and 2003, respectively, and the Ph.D. degree in hydrology from the Massachusetts Institute of Technology, Cambridge, in 2008.

He is currently an Assistant Research Professor with the Geosciences Department, Boise State University, Boise, ID. His research interests include hydrologic data assimilation and applications, remote sensing of the hydrologic cycle, land surface ecohydrology, interactions between water, energy, carbon, and biogeochemical cycles, and fluvial geomorphology.

Valeriy Y. Ivanov received the Diploma from Moscow State University, Moscow, Russia, in 1996 and the S.M. and Ph.D. degrees in hydrology from the Massachusetts Institute of Technology, Cambridge, in 2002 and 2006, respectively.

He is currently an Assistant Professor with the Department of Civil and Environmental Engineering, University of Michigan, Ann Arbor. His research interests include land surface hydrology and ecohydrology, hydrosphere–biosphere interactions and carbon cycling, and data assimilation.

Dara Entekhabi (M'04–SM'04) received the B.A. and two M.A. degrees in geography from Clark University, Worcester, MA, in 1983, 1984, and 1987, respectively, and the Ph.D. degree in civil engineering from the Massachusetts Institute of Technology (MIT), Cambridge, in 1990.

He is currently a Professor with the Department of Civil and Environmental Engineering and the Department of Earth, Atmospheric, and Planetary Sciences, MIT. He is the Leader of the Science Definition Team for NASA's Soil Moisture Active-Passive mission. He is the Director of the Ralph M. Parsons Laboratory. His research activities are in terrestrial remote sensing, data assimilation, and coupled land–atmosphere systems behavior.

Prof. Entekhabi is a Fellow of the American Meteorological Society and the American Geophysical Union.

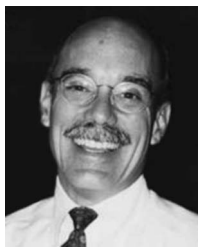

Rafael L. Bras received the B.S., S.M., and Sc.D. degrees in civil engineering from the Massachusetts Institute of Technology, Cambridge, in 1972, 1974, and 1975, respectively.

He is currently the Dean of the Henry Samueli School of Engineering, University of California, Irvine. From 1976 to 2008, he was a Professor with the Department of Civil and Environmental Engineering, MIT, where he held a joint appointment with the Department of Earth, Atmospheric, and Planetary Sciences from 1990 until 2008. From 1992 to 2001, he was the Head of the Department of Civil and Environmental Engineering. From 1983 to 1991, he was the Director of the Ralph M. Parsons Laboratory. His research activities include hydrometeorology, land–atmosphere interactions, rainfall-runoff modeling, and fluvial geomorphology.

Dr. Bras is a Fellow of the American Society of Civil Engineers, American Association for the Advancement of Science, the American Meteorological Society, and the American Geophysical Union and is a member of the National Academy of Engineering.